Article

Nanostructuring, Compositional Fluctuations, and Atomic Ordering in the Thermoelectric Materials AgPbSbTe. The Myth of Solid Solutions

Eric Quarez, Kuei-Fang Hsu, Robert Pcionek, N. Frangis, E. K. Polychroniadis, and Mercouri G. Kanatzidis

J. Am. Chem. Soc., **2005**, 127 (25), 9177-9190• DOI: 10.1021/ja051653o • Publication Date (Web): 04 June 2005

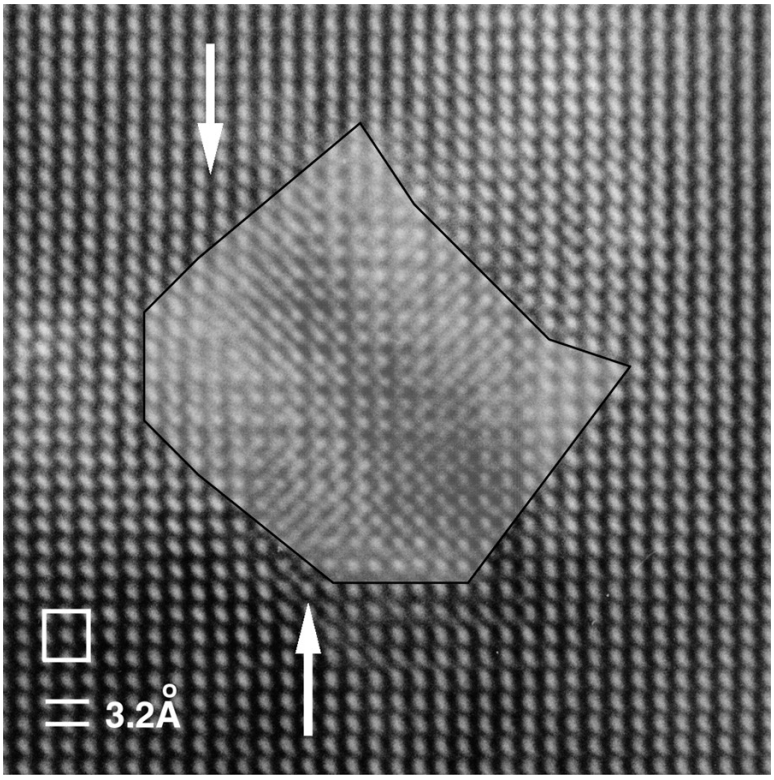

J|A|C|S
ARTICLES
Published on Web 06/04/2005

Nanostructuring, Compositional Fluctuations, and Atomic Ordering in the Thermoelectric Materials $AgPb_mSbTe_{2+m}$. The Myth of Solid Solutions

Eric Quarez,[†] Kuei-Fang Hsu,[†] Robert Pcionek,[†] N. Frangis,[‡] E. K. Polychroniadis,[‡] and Mercouri G. Kanatzidis*,[†]

Contribution from the Department of Chemistry, Michigan State University, East Lansing, Michigan 48824, and Solid State Physics Section, Department of Physics, Aristotle University of Thessaloniki, GR-54124 Thessaloniki, Greece

Received March 15, 2005; E-mail: kanatzid@cem.msu.edu

Abstract: The nature of the thermoelectric materials $Ag_{1-x}Pb_mSbTe_{m+2}$ or LAST-*m* materials (LAST for Lead Antimony Silver Tellurium) with different *m* values at the atomic as well as nanoscale was studied with powder/single-crystal X-ray diffraction, electron diffraction, and high-resolution transmission electron microscopy. Powder diffraction patterns of different members ($m = 0$, 6, 12, 18, ∞) are consistent with pure phases crystallizing in the NaCl-structure-type ($Fm\bar{3}m$) and the proposition that the LAST family behaved as solid solutions between the PbTe and $AgSbTe_2$ compounds. However, electron diffraction and high resolution transmission electron microscopy studies suggest the LAST phases are inhomogeneous at the nanoscale with at least two coexisting sets of well-defined phases. The minority phase which is richer in Ag and Sb is on the nanosized length scale, and it is endotaxially embedded in the majority phase which is poorer in Ag and Sb. Moreover, within each nanodomain we observe extensive long range ordering of Ag, Pb, and Sb atoms. The long range ordering can be confirmed by single crystal X-ray diffraction studies. Indeed, data collections of five different single crystals were successfully refined in space groups of lower symmetry than $Fm\bar{3}m$ including $P4/mmm$ and $R\bar{3}m$. The results reported here provide experimental evidence for a conceptual basis that could be employed when designing high performance thermoelectric materials and dispel the decades long belief that the systems $(AgSbTe_2)_{1-x}(PbTe)_x$ are solid solutions.

Introduction

Thermoelectric materials are becoming increasingly important in the field of energy production, conversion, and conservation. The past decade has been a strong interest to enhance the thermoelectric performance of materials to achieve a figure of merit (ZT)[1] higher than the critical value of $\sim$1.[2−5] Some recent reports have claimed that nanostructured thin-film superlattices of Bi_2Te_3 and Sb_2Te_3, grown from chemical vapor deposition, have ZT $\approx$ 2.4 at room temperature,[3] whereas $PbSe_{0.98}Te_{0.02}$/PbTe quantum dot superlattices grown by molecular beam epitaxy have ZT $\approx$ 1.6.[4] In this latter publication, the thin-film $PbSe_{0.98}Te_{0.02}$/PbTe systems feature pyramidal-shaped nanodots of PbSe embedded in a PbTe matrix material. At high temperatures ($\sim$550 K), these samples are reported to exhibit ZT $\approx$ 2.5. The primary reason for the very high values of ZT appears to be a very marked depression of the system's thermal conductivity.

Recently, we described the family of chalcogenide lead-based compounds, $AgPb_mSbTe_{m+2}$, or LAST-*m* materials (LAST for Lead Antimony Silver Tellurium), several members of which exhibit large ZT values from $\sim$1.2 (LAST-10) to $\sim$2.2 (LAST-18) at 800 K.[5,6] Preliminary electron microscopic examination

[†] Michigan State University.
[‡] Aristotle University of Thessaloniki.

(1) ZT is defined as $ZT = \sigma S^2 T/\kappa$, where σ is the electrical conductivity, *S* is the thermopower or Seebeck coefficient, κ is the thermal conductivity, and *T* is the absolute temperature. The numerator (σS^2) is called the power factor.

(2) (a) Ohtaki, M.; Ogura, D.; Eguchi, K.; Arai, H. *J. Mater. Chem.* **1994**, *4*, 653−6. (b) Sales, B. C.; Mandrus, D.; Williams, R. K. *Science* **1996**, *272*, 1325−1328. (c) Chung, D.-Y.; Choi, K.-S.; Iordanidis, L.; Schindler, J. L.; Brazis, P. W.; Kannewurf, C. R.; Chen, B.; Hu, S.; Uher, C.; Kanatzidis, M. G. *Chem. Mater.* **1997**, *9*, 3060−3071. (d) Chung, D.-Y.; Hogan, T.; Brazis, P.; Rocci-Lane, M.; Kannewurf, C.; Bastea, M.; Uher, C.; Kanatzidis, M. G. *Science* **2000**, *287*, 1024−1027. (e) Nolas, G. S.; Kaeser, M.; Littleton, R., IV; Tritt, T. M. *Appl. Phys. Lett.* **2000**, *77*, 1822. (f) Imai, H.; Shimakawa, Y.; Kubo, Y. *Phys. Rev. B* **2001**, *64*, 241104/1−241104/4. (g) Kanatzidis, M. G. *Semicond. Semimet.* **2001**, *69*, 51−100. (h) Meng, J. F.; Shekar, N. V. C.; Badding, J. V.; Chung, D. Y.; Kanatzidis, M. G. *J. Appl. Phys.* **2001**, *90*, 2836−2839. (i) Polvani, D. A.; Meng, J. F.; Shekar, N. V. C.; Sharp, J.; Badding, J. V. *Chem. Mater.* **2001**, *13*, 2068−2071. (j) Wolfing, B.; Kloc, C.; Teubner, J.; Bucher, E. *Phys. Rev. Lett.* **2001**, *86*, 4350−4353. (k) Larson, P.; Mahanti, S. D.; Chung, D. Y.; Kanatzidis, M. G. *Phys. Rev. B* **2002**, *65*, 045205/1−045205/5. (l) Maignan, A.; Wang, L. B.; Hebert, S.; Pelloquin, D.; Raveau, B. *Chem. Mater.* **2002**, *14*, 1231−1235. (m) Zhu, P. W.; Jia, X.; Chen, H. Y.; Chen, L. X.; Guo, W. L.; Mei, D. L.; Liu, B. B.; Ma, H. A.; Ren, G. Z.; Zou, G. T. *Chem. Phys. Lett.* **2002**, *359*, 89−94. (n) Vashaee, D.; Shakouri, A. *Phys. Rev. Lett.* **2004**, *92*, 106103.
(3) Venkatasubramanian, R.; Siivola, E.; Colpitts, T.; O'Quinn, B. *Nature* **2001**, *413*, 597−602.
(4) Harman, T. C.; Taylor, P. J.; Walsh, M. P.; LaForge, B. E. *Science* **2002**, *297*, 2229−2232.
(5) Hsu, K. F.; Loo, S.; Guo, F.; Chen, W.; Dyck, J. S.; Uher, C.; Hogan, T.; Polychroniadis, E. K.; Kanatzidis, M. G. *Science* **2004**, *303*, 818−821.
(6) (a) A recent report on polycrystalline compactions of LAST-18 samples is consistent with the high performance nature of the thermoelectric properties of these materials (a ZT of 1 at 675 K vs 1.5 for single-crystal ingot at the same temperature). (b) Kosuga, A.; Uno, M.; Kurosaki, K.; Yamanaka, S. *J. Alloy Compd.* **2005**, *391*, 288−291.

Table 1. X-ray Intensity and Analytical Data for Single Crystals of $AgSbTe_2$, $Ag_{1.33}Pb_{1.33}Sb_{1.33}Te_4$, $Ag_{0.5}Pb_3Sb_{0.5}Te_4$, $Ag_{0.38}Pb_{3.23}Sb_{0.38}Te_4$, and $Ag_{0.25}Pb_{3.5}Sb_{0.25}Te_4$

composition from XRD refinements (EDS analyses)	*m* value	no. total reflections	no. reflections violating F-centering	selected reflections	1 0 0	2 0 0	3 1 1	3 3 1
				approximate 2θ (deg)	13.8	27.7	46.9	62.8
$AgSbTe_2$ ($Ag_{0.91}Sb_{1.04}Te_2$)	0	8159	6121	relative intensity	3	8736	167	159
$Ag_{1.33}Pb_{1.33}Sb_{1.33}Te_4$ ($Ag_{1.21}Pb_{1.12}Sb_{1.44}Te_4$)	1	2175	1631		37	9843	82	52
$Ag_{0.5}Pb_3Sb_{0.5}Te_4$ ($Ag_{0.38}Pb_{3.15}Sb_{0.46}Te_4$)	6	2297	1739		23	9313	277	170
$Ag_{0.38}Pb_{3.23}Sb_{0.38}Te_4$ ($Ag_{0.32}Pb_{3.30}Sb_{0.34}Te_4$)	17	2247	1718		108	8091	438	291
$Ag_{0.25}Pb_{3.5}Sb_{0.25}Te_4$ ($Ag_{0.18}Pb_{3.60}Sb_{0.22}Te_4$)	14	3037	2297		42	9269	387	243

of these samples revealed endotaxially[7] dispersed quantum dots (i.e., regions 2 to 4 nm in size that are rich in Ag−Sb and are surrounded by a PbTe matrix) similar to those found in the PbSe/PbTe thin films. This is a significant observation and raises important new questions as to the possible significance and impact of these nanostructural features on the thermoelectric properties.

Following this discovery, we initiated studies to explain the large ZT value and begun with electronic structure calculations on various LAST compositions. The calculations reveal resonant states near the Fermi level and suggest that microstructural arrangements of Ag/Sb atoms in a PbTe matrix may play a role in the enhancement of the thermoelectric properties by impacting the power factor.[8]

We have now embarked on extensive TEM studies to fully characterize the LAST materials on the atomic scale and probe the extent and nature of nanostructuring. In this article, we present some of our first results of these studies.

Many articles dealing with solid solutions between $AgSbTe_2$ and binary compounds such as PbTe, SnTe, and GeTe have been reported in the literature. In these early reports, it was generally concluded that solid solutions exist between $AgSbTe_2$ and PbTe,[9−13] $AgSbTe_2$ and GeTe,[10,14] and $AgSbTe_2$ and SnTe[10,11,15] systems, although no structural characterization beyond basic X-ray powder diffraction experiments and the verification of "Vegard's law" were performed. In the present article, we present direct proof that samples of the formula $AgSbTe_2 - m$PbTe (i.e., $AgPb_mSbTe_{m+2}$) are not solid solutions but exhibit extensive nanostructuring caused by compositional fluctuations. Within individual domains long-range atomic ordering is observed giving rise to symmetry lowering and superstructures. The implications of these results on understanding the thermoelectric properties of the $AgPb_mSbTe_{m+2}$ materials but also bulk materials in general are strong.

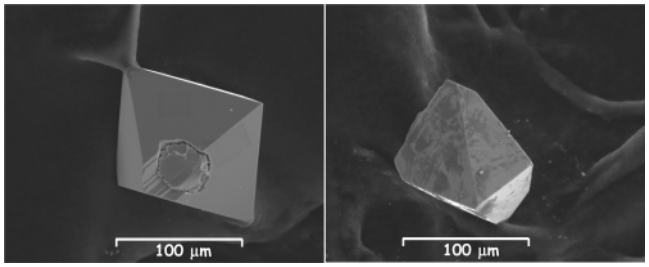

Figure 1. SEM images of single crystals of $Ag_{1.33}Pb_{1.33}Sb_{1.33}Te_4$ (left) and $Ag_{0.5}Pb_3Sb_{0.5}Te_4$ (right).

Experimental Section

Synthesis. Ingots with nominal compositions of $AgPb_6SbTe_8$, $AgPb_{12}SbTe_{14}$, $Ag_{0.95}Pb_{15}SbTe_{17}$, $AgPb_{18}SbTe_{20}$, and $Ag_{0.86}Pb_{18}SbTe_{20}$ were prepared by annealing, in quartz tubes under vacuum, mixtures of Ag, Pb, Sb, and Te at 950 °C for 4 h and cooling to 450 °C in 40 h. $AgSbTe_2$ and PbTe were synthesized by annealing appropriate stoichiometric ratios of the elements at 800 and 1000 °C, respectively.

Single crystals with suitable size for X-ray characterization were obtained by evaporation during annealing except for single crystals of $AgSbTe_2$ that were obtained from the ingot. $AgSbTe_2$ single crystals were prepared by cooling from 650 °C to room temperature at 5 °C/h rate. In the cases of single crystals obtained by evaporation, the observed compositions were different from the nominal compositions as evaporation at these temperatures is not congruent. $Ag_{0.5}Pb_3Sb_{0.5}Te_4$, $Ag_{0.38}Pb_{3.23}Sb_{0.38}Te_4$, and $Ag_{0.25}Pb_{3.5}Sb_{0.25}Te_4$ single crystals were obtained by synthesizing $m = 1$, $m = 17$, and $m = 18$ compounds, respectively. $Ag_{1.33}Pb_{1.33}Sb_{1.33}Te_4$ single crystals were grown by annealing at 1000 °C a mixture of $AgSbTe_2$ and PbTe and cooling at a 20 °C/h rate. Single crystals generally adopted a square bypyramidal shape or sometimes more complex polyhedral shapes; see Figure 1.

EDS Analysis. Semiquantitative microprobe analyses of the single crystals were performed with a JEOL JSM-35C scanning electron microscope (SEM) equipped with a Tracor Northen energy dispersive spectrometer (EDS). Data were acquired using an accelerating voltage of 25 kV and a 30 s accumulation time. The analyses on the five single crystals used for X-ray diffraction agreed quite well with the atomic ratios that were derived from the final refinements (Table 1).

Powder X-ray Diffraction. Powder X-ray diffractograms of the crushed $AgPb_6SbTe_8$, $AgPb_{12}SbTe_{14}$, $AgPb_{18}SbTe_{20}$, $Ag_{0.86}Pb_{18}SbTe_{20}$, $AgSbTe_2$, and PbTe compounds were recorded on a Rigaku Rotaflex RTP 300RC rotating-anode equipped with powder theta − 2 theta diffractometer using Kα radiation and Bragg Brentano geometry and operating at 45 kV and 100 mA.

(7) By the use of the term "endotaxy" we mean the disposition of a nanocrystalline particle inside a solid crystalline matrix with coherent defect-free interfaces on its entire surface.

(8) Bilc, D.; Mahanti, S. D.; Quarez, E.; Hsu, K.-F.; Pcionek, R.; Kanatzidis, M. G. *Phys. Rev. Lett.* **2004**, *93*, 146403/1−146403/4.
(9) (a) Rodot, H. *Compt. Rend.* **1959**, *249*, 1872−4. (b) Borissova, L. D.; Dimitrova, S. K. *Bulg. J. Phys.* **1975**, *2*, 50−7. (c) Borisova, L. *Phys. Status Solidi B* **1984**, **126**, K155−K158. (d) Borisova, L. *Bulg. J. Phys.* **1986**, *13*, 43−52.
(10) (a) Rosi, F. D.; Hockings, E. S.; Lindenblad, N. E. *Adv. Energy Convers.* **1961**, *1*, 151. (b) Rosi, F. D. *Mater. Sci. Technol. Adv. Appl.* **1962**, 408−30. (c) Fleischmann, H.; Luy, H. *Z. Naturforsch., A: Phys. Sci.* **1963**, *18*, 646−9.
(11) Ono, T.; Takahama, T.; Irie, T. *J. Phys. Soc. Jpn.* **1962**, *17*, 1070−1.
(12) Borisova, L.; Decheva, S.; Dimitrova, S.; Moraliiski, P. *God. Sofii. Univ. "Sv. Kliment Okhridski", Fiz. Fak.* **1973**, 167−76.
(13) Pabst, A. *Can. Mineral.* **1976**, *14*, Pt. 4, 503−7.
(14) (a) Decheva-Plachkova, S. *Phys. Status Solidi B* **1983**, *119*, K97−K100. (b) Plachkova, S. K.; Odin, I. N. *Izv. Akademii Nauk, Neorg. Mater.* **1983**, *19*, 588−92. (c) Plachkova, S. *Phys. Status Solidi A* **1984**, *83*, 349−55.
(15) Ishihara, T. *J. Phys. Soc. Jpn.* **1962**, *17*, 719−20.

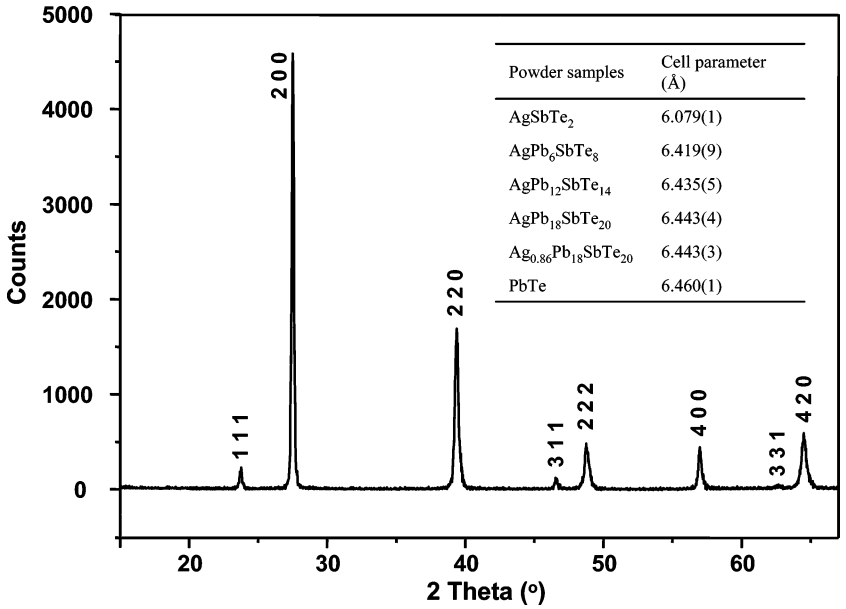

Figure 2. Typical example of X-ray powder diffraction pattern obtained for $AgPb_6SbTe_8$, $AgPb_{12}SbTe_{14}$, $AgPb_{18}SbTe_{20}$, $Ag_{0.86}Pb_{18}SbTe_{20}$, $AgSbTe_2$, and PbTe compounds. The inset presents the refined cell parameters for the above-mentioned phases. These patterns are consistent with an $Fm\bar{3}m$ structure since the very weak reflections indicative of the true primitive lattice are not observed.

The X-ray powder diffraction (XRD) patterns show "single phase" crystallizing in a cubic F lattice (NaCl-type) with refined cell parameters indicated in the Figure 2. These patterns showed no evidence of violation of the F-centering condition (i.e. P lattice) at the X-ray Rigaku diffractometer detection limit. As we will show later, these materials are in fact not single phases but multiple phases and the powder XRDs represent an average of all.

Single-Crystal X-ray Diffraction. For the single crystal of $AgSbTe_2$, intensity data were collected at 273 K using graphite-monochromatized Mo Kα radiation ($\lambda = 0.710\ 73$ Å), on a STOE IPDS-II diffractometer. Crystal data and further details of the data collection are given in Table 2. A numerical absorption correction to the data was applied with the program X-RED[16] based on a crystal shape description determined using equivalent reflections with X-SHAPE.[17]

For the single crystals of $Ag_{1.33}Pb_{1.33}Sb_{1.33}Te_4$, $Ag_{0.5}Pb_3Sb_{0.5}Te_4$, $Ag_{0.38}Pb_{3.23}Sb_{0.38}Te_4$ and $Ag_{0.25}Pb_{3.5}Sb_{0.25}Te_4$, X-ray diffraction intensities were collected at room temperature on a Bruker SMART Platform CCD diffractometer using a graphite-monochromatized Mo Kα radiation under conditions shown in Tables 2 and 3. Total spheres of reciprocal space (4 × 606 frames) were collected by using ω-scans, 20 s per frame, 0.3° oscillations for four different values of φ (0°, 90°, 180°, and 270°), and a crystal-to-detector distance of 50 mm. The SMART software[18] was used for the data acquisition, and SAINT,[19] for data extraction and reduction. An absorption correction based on face indexation was then applied using the program Xprep of the SHELXTL package.[20] An additional correction for absorption based on symmetry equivalent reflections was subsequently applied with the program SADABS.[21]

The structure solution and refinements were performed with the SHELXTL software. The complete data collection parameters and details of the structure refinement are given in Tables 2 and 3.

Crystal Structure Refinements. $AgSbTe_2$ and $Ag_{1.33}Pb_{1.33}Sb_{1.33}Te_4$: The crystal structure of $AgSbTe_2$ and $Ag_{1.33}Pb_{1.33}Sb_{1.33}Te_4$ reported in the literature[12,22] indicates that the phases adopt the cubic NaCl-type structure ($Fm\bar{3}m$ space group) with Te in position 4a (0, 0, 0) and Ag and Sb atoms (plus Pb for $Ag_{1.33}Pb_{1.33}Sb_{1.33}Te_4$) indistinguishable in position 4b ($^1/_2$, $^1/_2$, $^1/_2$). In our present study, we observe that the diffraction data are not consistent with an F-centered lattice but a primitive lattice. Refinements in the $Fm\bar{3}m$ space group led to the omission of almost 40% of observed reflections that violate the F lattice (Table 1). Thus, the refinements were carried out in the $Pm\bar{3}m$ space group (Te atoms are located in two different sites ((1a) 0, 0, 0; (3c) 0, $^1/_2$, $^1/_2$) and Ag, Sb, and Pb atoms in two other sites ((1b) $^1/_2$, $^1/_2$, $^1/_2$; (3d) $^1/_2$, 0, 0)). This violation of the F lattice was systematically observed for every single crystal we examined. By selecting $Pm\bar{3}m$, all observed reflections could be taken into account in the refinement.

However a lower symmetry tetragonal model with a smaller unit cell is also suitable in describing the crystal structure. Thus, data of $AgSbTe_2$ and $Ag_{1.33}Pb_{1.33}Sb_{1.33}Te_4$ were also refined in the $P4/mmm$ space group. The volume of the tetragonal unit cell ($a = b \approx a_c\sqrt{2}/2$, $c \approx a_c$) is half of the cubic one, but as in the case of the cubic P unit cell, two independent sites can be possibly occupied by Ag and Sb atoms plus Pb in the case of $Ag_{1.33}Pb_{1.33}Sb_{1.33}Te_4$ ((1b) 0, 0, $^1/_2$; (1c) $^1/_2$, $^1/_2$, 0). For $AgSbTe_2$, it was also possible to find an ordered trigonal model (centrosymmetric $R\bar{3}m$ space group) in which the Ag and Sb layers alternate with the Te layers along the *c*-axis. The tetragonal models gave better refinement results than the cubic ones and only slightly better than trigonal models.[23]

$AgPb_mSbTe_{m+2}$ ($m > 1$): Again in this family of compounds we found strong evidence for a primitive lattice rather than an F-centered lattice. The refinements for $Ag_{0.5}Pb_3Sb_{0.5}Te_4$, $Ag_{0.38}Pb_{3.23}Sb_{0.38}Te_4$, and $Ag_{0.25}Pb_{3.5}Sb_{0.25}Te_4$ were also carried out in $Pm\bar{3}m$ and in $P4/mmm$ space groups (Table 3).

One of the difficulties in solving these structures was the mixed occupancy sites containing different atoms: Ag and Sb for $AgSbTe_2$ and Ag, Sb and Pb for $AgPb_mSbTe_{m+2}$. Several approaches were

(16) *X-RED 1.22, Program for data reduction*; STOE & Cie: Darmstadt, Germany, 2001.
(17) *X-SHAPE 1.06, Program for crystal optimization for numerical absorption correction*; STOE & Cie: Darmstadt, Germany 1999.
(18) *SMART;* Siemens Analytical X-ray Systems, Inc.: Madison, WI 53719, 1994.
(19) *SAINT + version 6.02: Area-Detector Integration Software*; Siemens Industrial Automation, Inc.: Madison, WI 1998.
(20) Sheldrick, G. M. *SHELXTL NT*, version 5.1; Bruker Analytical X-ray Systems: 1998.
(21) *SADABS: Area-Detector Absorption Correction*; Siemens Industrial Automation, Inc.: Madison, WI, 1996.
(22) Geller, S.; Wernick, J. H. *Acta Crystallogr.* **1959**, *12*, 46−54.
(23) Some attempts to refine the data of the single crystal of $AgPbSbTe_3$ were performed by considering an ordered model in which Ag, Pb, and Sb atoms form layers alternating with Te layers ($P3m1$ space group, $a = 4.3963(6)$ Å, $c = 10.769(2)$ Å), but this solution was not kept because the final refinement did not yield a significant improvement of the reliability factors.

Table 2. Crystal, Data Collection, and Details of Structure Refinement for $AgSbTe_2$ and $Ag_{1.33}Pb_{1.33}Sb_{1.33}Te_4$

	$AgSbTe_2$			$Ag_{1.33}Pb_{1.33}Sb_{1.33}Te_4$	
crystal symmetry	cubic	tetragonal	trigonal	cubic	tetragonal
space group	$Pm\bar{3}m$ (no. 221)	$P4/mmm$ (no. 123)	$R3m$ (no. 166)	$Pm\bar{3}m$ (no. 221)	$P4/mmm$ (no. 123)
unit cell (Å)	$a = 6.0667(9)$	$a = 4.2898(6)$	$a = 4.2898(6)$	$a = 6.2173(8)$	$a = 4.3963(6)$
		$c = 6.0667(12)$	$c = 21.016(4)$		$c = 6.2173(12)$
volume (Å^3)	223.28(6)	111.64(3)	334.93(9)	240.33(5)	120.16(3)
Z	2	1	3	1	1
calculated density (g/cm^3)	7.211	7.211	7.211	7.551	7.551
equipment		STOE IPDS-II		Bruker SMART CCD-1K	
radiation Mo Kα (Å)	0.71073	0.71073	0.71073	0.71073	0.71073
scan mode	ω-scan	ω-scan	ω-scan	ω-scan	ω-scan
recording angular range 2θ (deg)	9.50−77.02	9.50−77.02	11.14−76.12	6.56−58.02	6.56−58.02
recording reciprocal space	$-10 \le h \le 10$	$-7 \le h \le 6$	$-7 \le h \le 7$	$-8 \le h \le 8$	$-6 \le h \le 5$
	$-10 \le k \le 10$	$-7 \le k \le 7$	$-7 \le k \le 7$	$-8 \le k \le 8$	$-5 \le k \le 5$
	$-10 \le l \le 10$	$-10 \le l \le 10$	$-35 \le l \le -36$	$-8 \le l \le 8$	$-8 \le l \le 8$
number of measured reflections	8159	4081	3469	2175	1085
number of independent reflections $[I > 2\sigma(I)]$	165	225	267	93	124
R merging factor	5.48	4.69	4.89	2.32	1.84
μ (mm^{-1})	23.020	23.020	23.019	41.476	41.477
crystal size (mm^3)	0.134 × 0.061 × 0.052			0.155 × 0.073 × 0.058	
transmission factor range	0.207−0.301			0.040−0.089	
refinement parameters					
number of refined parameters/constrains	6/1	8/0	6/0	6/2	6/2
goodness-of-fit on F^2	1.14	1.12	1.11	1.18	1.03
twin (volume ratio %)		1.0(0.1)/1.0(0.1)[a]			
R_1 (F)[b] $[I > 2\sigma(I)]$ (%)	4.30	2.79	2.84	1.57	1.12
wR_2 (F^2)[c] $[I > 2\sigma(I)]$ (%)	16.87	8.31	9.38	4.77	3.23
$w = 1/[\sigma^2(F_o^2) + (A \times P)^2 + B \times P]$	$A = 0.0755$	$A = 0.0405$	$A = 0.0477$	$A = 0.0$	$A = 0.0$
with $P = [\max(F_o^2,0) + 2F_c^2)]/3$	$B = 0.7536$	$B = 0.2070$	$B = 3.0469$	$B = 4.8202$	$B = 0.5833$
isotropic secondary extinction	0.8(1)	0.93(9)	0.15(2)	0.012(1)	0.044(4)
max/min $\Delta\rho$ e/Å^3	2.04/−1.11	1.05/−0.82	1.55/−0.95	0.41/−0.67	0.37/−0.36

[a] Application of twin laws inversing the a- and c-axis and b- and c-axis of the tetragonal unit cell permitted to lower the R factors only significant in the case of the crystal structure of $AgSbTe_2$. [b] R_1 $(F) = \sum ||F_o| - |F_c||/\sum |F_o|$. [c] wR_2 $(F^2) = [\sum w(F_o^2 - F_c^2)^2/\sum w(F_o^2)]^{1/2}$.

investigated to determine the best way to refine the structures. We give here the method we applied to solve the crystal structure of the quaternary samples in the tetragonal $P4/mmm$ space group, but identical approaches were applied for all refinements.

The approach we found to provide a satisfactory solution was to consider linear functions constraining the Ag, Sb, and Pb atoms on the various sites. The first type of function was to constrain the sum of site occupation factors (SOF) in the cations sites to be equal to 1 (i.e., sites 1b and 1c fully occupied). The second type of constrain was to consider the sum of the formal charge of Ag, Pb, and Sb atoms multiplied by their own SOF equal to 2 (i.e., average charge = +2). To do so, it was necessary to assign to the mixed sites a multiplicity of 2 (instead of 1) and to restrain in the linear functions the occupation of mixed sites at 50%. Thus, six new free variables were added (four in the case of $AgSbTe_2$) and refined using initial values consistent with the compositions of the compounds. Moreover, the atoms sharing the same site were constrained to have identical thermal parameters.

The structure refinements in a highly symmetric space group (especially cubic) generally imply a small number of independent reflections leading to a ratio: number of refined parameters over number of independent reflections close to the limit for an acceptable structure refinement. In this matter and to help the system converge during the refinement, a damping factor of 5000 was introduced and then slightly decreased until it was finally completely removed in the final cycles of refinement. In the last cycles of refinement, the occupation of mixed sites were reassigned to their normal value and the SOFs of Ag, Pb, and Sb atoms were fixed.

Finally, the secondary extinction and an optimized weighting scheme were introduced leading to the final reliability factors reported in Tables 2 and 3. The formulas obtained after refinements were $AgSbTe_2$, $Ag_{1.33}Pb_{1.33}Sb_{1.33}Te_4$, $Ag_{0.5}Pb_3Sb_{0.5}Te_4$, $Ag_{0.38}Pb_{3.23}Sb_{0.38}Te_4$, and $Ag_{0.25}Pb_{3.5}Sb_{0.25}Te_4$. In the formula scheme of $AgPb_mSbTe_{m+2}$, these compounds are formally $AgSbTe_2$ ($m = 0$), $AgPbSbTe_3$ ($m = 1$), $AgPb_6SbTe_8$ ($m = 6$), $AgPb_{8.5}SbTe_{10.5}$ ($m = 8.5$), and $AgPb_{14}SbTe_{16}$ ($m = 14$). The refined atomic coordinates and isotropic displacement parameters are presented in Table 4.

Electron Diffraction Study. TEM samples were first obtained by three different ways: some were produced by cutting the slabs with a diamond saw (model 850, South Bay Technology), others were just trimmed by cleaving with a razor blade, and in some cases, disks were cut using a Gatan model 601 ultrasonic disk cutter. Then, these slabs were thinned using a Gatan model 656 precision dimple grinder and then low-angle ion milled (2°−4°) to electron transparency using a Gatan model 691 precision ion polishing system (PIPS). Electron diffraction patterns were produced at 100 kV with a JEOL 100CX transmission electron microscope (TEM). Experimental diffraction patterns were compared to those calculated using CERIUS^2 software package.[24]

High-Resolution TEM Study. High-resolution transmission electron microscopy images were obtained at 200 kV using a JEOL JEM 2200FS (Field emission TEM), as well as a JEOL 2011 transmission electron microscope. A fast Fourier transform (FFT) image was accomplished by capturing selected areas of a square, power of two size image (128 × 128 pixels) and processing it with the Scion NIH image software.[25]

Results and Discussion

The LAST materials were prepared and characterized by different techniques. Although powder X-ray diffraction suggests that these systems behave as solid solutions between $AgSbTe_2$ and PbTe (Vegard's law is generally obeyed), our single-crystal X-ray diffraction, electron diffraction studies and high-resolution

(24) *Cerius*^{2}, version 3.8; Molecular Simulations, Inc.: San Diego, CA, 1998.
(25) *Scion Image for Windows*, version 4.0.2; Scion Corporation, Maryland, USA 2000.

Table 3. Crystal, Data Collection, and Details of Structure Refinement for $Ag_{0.5}Pb_3Sb_{0.5}Te_4$, $Ag_{0.38}Pb_{3.23}Sb_{0.38}Te_4$, and $Ag_{0.25}Pb_{3.5}Sb_{0.25}Te_4$

	$Ag_{0.5}Pb_3Sb_{0.5}Te_4$		$Ag_{0.38}Pb_{3.23}Sb_{0.38}Te_4$		$Ag_{0.25}Pb_{3.5}Sb_{0.25}Te_4$	
crystal symmetry	cubic	tetragonal	cubic	tetragonal	cubic	tetragonal
space group	$Pm\bar{3}m$ (no. 221)	$P4/mmm$ (no. 123)	$Pm\bar{3}m$ (no. 221)	$P4/mmm$ (no. 123)	$Pm\bar{3}m$ (no. 221)	$P4/mmm$ (no. 123)
unit cell (Å)	$a = 6.4173(8)$	$a = 4.5377(6)$ $c = 6.4173(13)$	$a = 6.4280(11)$	$a = 4.5453(6)$ $c = 6.4280(13)$	$a = 6.4404(12)$	$a = 4.5538(6)$ $c = 6.4404(14)$
volume (Å^3)	264.28(6)	132.14(4)	265.60(8)	132.80(4)	267.14(9)	133.56(4)
Z	1	1	1	1	1	1
calculated density (g/cm^3)	7.834	7.834	7.910	7.910	8.037	8.038
equipment	Bruker SMART CCD-1K		Bruker SMART CCD-1K		Bruker SMART CCD-1K	
radiation Mo Kα (Å)	0.71073	0.71073	0.71073	0.71073	0.71073	0.71073
scan mode	ω-scan	ω-scan	ω-scan	ω-scan	ω-scan	ω-scan
recording angular range 2θ (deg)	6.34−56.90	6.34−56.06	6.34−56.80	6.34−56.80	9.50−77.02	9.50−77.02
recording reciprocal space	$-8 \le h \le 8$ $-8 \le k \le 8$ $-8 \le l \le 8$	$-5 \le h \le 5$ $-5 \le k \le 5$ $-8 \le l \le 8$	$-8 \le h \le 8$ $-8 \le k \le 8$ $-8 \le l \le 8$	$-5 \le h \le 5$ $-5 \le k \le 5$ $-8 \le l \le 8$	$-8 \le h \le 8$ $-8 \le k \le 8$ $-8 \le l \le 8$	$-6 \le h \le 5$ $-5 \le k \le 5$ $-8 \le l \le 8$
number of measured reflections	2297	1136	2247	1102	3037	1499
number of independent reflections $[I > 2\sigma(I)]$	93	125	96	126	97	126
R merging factor	4.57	3.70	5.52	5.02	6.19	5.26
μ (mm^{-1})	60.554	60.555	62.979	62.978	66.682	66.690
crystal size (mm^3)	0.130 × 0.057 × 0.045		0.241 × 0.103 × 0.060		0.129 × 0.055 × 0.039	
transmission factor range	0.019−0.066		0.001−0.025		0.022−0.082	
refinement parameters						
number of refined parameters/constrains	6/2	6/2	6/1	6/1	6/1	6/1
goodness-of-fit on F^2	1.17	1.19	1.30	1.22	1.12	1.06
R_1 (F) $[I > 2\sigma(I)]$ (%)[a]	2.73	2.47	2.71	2.37	2.08	2.09
wR_2 (F^2) $[I > 2\sigma(I)]$ (%)[b]	5.40	4.95	8.12	7.30	4.72	4.69
$w = 1/[\sigma^2(F_o^2) + (A \times P)^2 + B \times P]$	$A = 0.0$	$A = 0.0$	$A = 0.0232$	$A = 0.0270$	$A = 0.0755$	$A = 0.0$
with $P = [\max(F_o^2,0) + 2F_c^2)]/3$	$B = 33.7272$	$B = 5.3138$	$B = 9.9285$	$B = 1.5451$	$B = 0.7536$	$B = 4.8956$
isotropic secondary extinction	0.0013(4)	0.004(1)	0.012(2)	0.046(6)	0.0024(4)	0.009(1)
max/min $\Delta\rho$ e/Å^3	1.37/−1.51	1.09/−1.13	1.44/−1.24	1.47/−1.08	0.95/−1.00	1.33/−1.03

[a] $R_1\ (F) = \sum ||F_o| - |F_c||/\sum |F_o|$. [b] $wR_2\ (F^2) = [\sum w(F_o^2 - F_c^2)^2/\sum w(F_o^2)]^{1/2}$.

Table 4. Atomic Parameters and Equivalent Isotropic Displacement Parameters for $AgSbTe_2$ ($m = 0$), $Ag_{1.33}Pb_{1.33}Sb_{1.33}Te_4$ ($m = 1$), $Ag_{0.5}Pb_3Sb_{0.5}Te_4$ ($m = 6$), $Ag_{0.38}Pb_{3.238}Sb_{0.38}Te_4$ ($m = 8.5$), and $Ag_{0.25}Pb_{3.5}Sb_{0.25}Te_4$ ($m = 14$) (U_{eq} Is Defined as One-Third of the Trace of the Orthogonalized U^{ij} Tensor)

	atoms	site	occupancy	x	y	z	U_{eq} (Å^2)
$AgSbTe_2$[a]	Te1	1a	1	0	0	0	0.029(1)
	Te2	1d	1	1/2	1/2	1/2	0.029(1)
	Sb	1b	1	0	0	1/2	0.045(1)
	Ag	1c	1	1/2	1/2	0	0.035(1)

	atoms	site	occupancy	x	y	z	U_{eq} (Å^2)
$Ag_{1.33}Pb_{1.33}Sb_{1.33}Te_4$[b]	Te1	1a	1	0	0	0	0.035(1)
	Te2	1d	1	1/2	1/2	1/2	0.035(1)
	Ag1/Pb1/Sb1	1b	0.17/0.42/0.41	0	0	1/2	0.044(1)
	Ag2/Pb2/Sb2	1c	0.50/0.24/0.26	1/2	1/2	0	0.033(1)

	atoms	site	occupancy	x	y	z	U_{eq} (Å^2)
$Ag_{0.5}Pb_3Sb_{0.5}Te_4$[c]	Te1	1a	1	0	0	0	0.025(1)
	Te2	1d	1	1/2	1/2	1/2	0.025(1)
	Ag1/Pb1/Sb1	1b	0.18/0.60/0.22	0	0	1/2	0.021(1)
	Ag2/Pb2/Sb2	1c	0.07/0.90/0.03	1/2	1/2	0	0.030(1)
$Ag_{0.38}Pb_{3.238}Sb_{0.38}Te_4$[d]	Te1	1a	1	0	0	0	0.025(1)
	Te2	1d	1	1/2	1/2	1/2	0.026(1)
	Ag1/Pb1/Sb1	1b	0.19/0.619/0.19	0	0	1/2	0.025(1)
	Ag2/Pb2/Sb2	1c	0.0/1.0/0.0	1/2	1/2	0	0.034(1)
$Ag_{0.25}Pb_{3.5}Sb_{0.25}Te_4$[e]	Te1	1a	1	0	0	0	0.018(1)
	Te2	1d	1	1/2	1/2	1/2	0.018(1)
	Ag1/Pb1/Sb1	1b	0.125/0.75/0.125	0	0	1/2	0.019(1)
	Ag2/Pb2/Sb2	1c	0.0/1.0/0.0	1/2	1/2	0	0.026(1)

[a] $AgSbTe_2$: $a = 4.2898(6)$Å, $c = 6.0667(12)$Å, $P4/mmm$ space group. [b] $Ag_{1.33}Pb_{1.33}Sb_{1.33}Te_4$: $a = 4.3963(6)$Å, $c = 6.2173(12)$Å, $P4/mmm$ space group. [c] $Ag_{0.5}Pb_3Sb_{0.5}Te_4$: $a = 4.5377(6)$Å, $c = 6.4173(13)$Å, $P4/mmm$ space group. [d] $Ag_{0.38}Pb_{3.23}Sb_{0.38}Te_4$: $a = 4.5453(6)$Å, $c = 6.4280(13)$Å, $P4/mmm$ space group. [e] $Ag_{0.25}Pb_{3.5}Sb_{0.25}Te_4$: $a = 4.5538(6)$Å, $c = 6.4404(14)$Å, $P4/mmm$ space group.

images reveal this is not the case. Depending on the m value and the experimental conditions used to prepare the materials, there exists both nanophase separation which creates a heterogeneous multiphasic system and long-range atomic ordering within the nanophases. We show this with single-crystal X-ray refinements coupled with TEM/HRTEM analysis. Here, we will

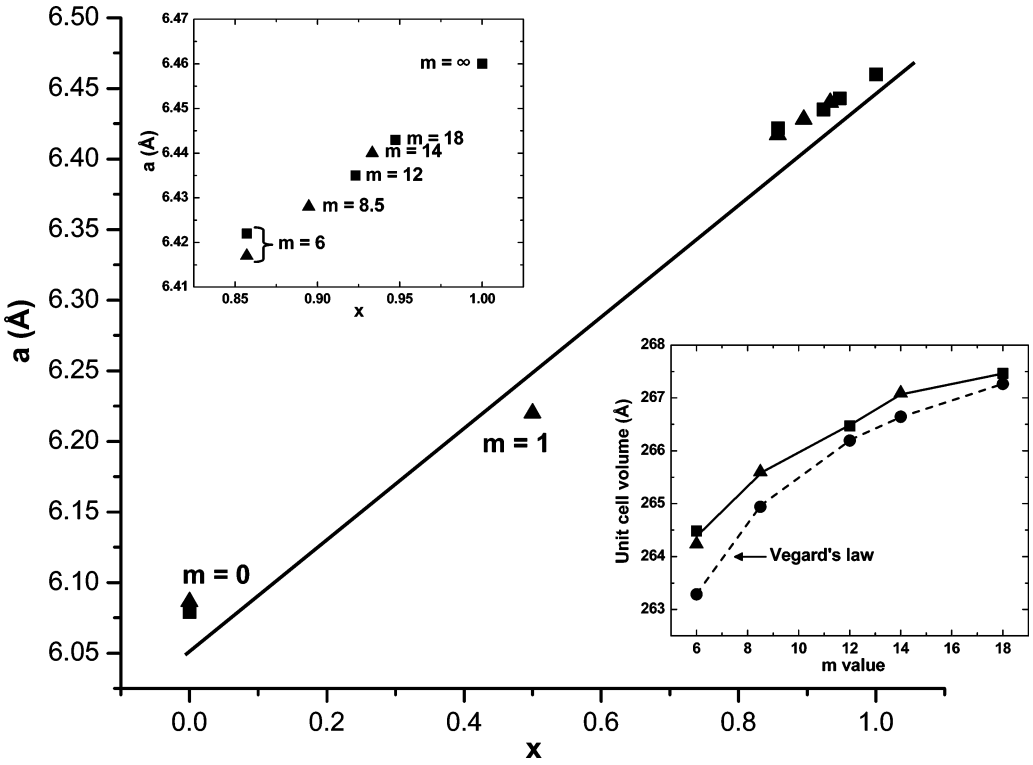

Figure 3. Plot of the *a* lattice parameter of $(AgSbTe_2)_{1-x}(PbTe)_x$ members as a function of x. Squares correspond to X-ray powder data whereas triangles correspond to single-crystal X-ray data. The data almost obey a linear fit. The inset at the top left presents magnification of the plot for *m* value ≥ 6. The inset at the bottom right presents the unit cell volume of samples from powder (■) and single crystals samples (▲) as a function of the *m* value ($m = 6$, 10, 12, and 18). The calculated Vegard's law is also plotted with $a = 6.079$ Å for $AgSbTe_2$ and 6.460 Å for PbTe according to $a^3 = (1 - x)a_{AgSbTe2}{}^3 + xa_{PbTe}{}^3$, where *a* stands for the cell parameter of the solid solution and *x* stands for the concentration.

not deal with samples prepared by quenching a melt which creates an apparent homogeneous sample along with a statistical disorder of all cations in the structure. This process leads to inferior thermoelectric properties.[26] Instead, we will focus on samples exhibiting generally high ZT values.

The formula $AgPb_mSbTe_{m+2}$ can be decomposed into two parts: PbTe m-fold and $AgSbTe_2$. The ternary compound was originally thought to have a cubic NaCl structure ($Fm\bar{3}m$ pace group) where the Ag and Sb atoms occupy statistically the Na sites.[22] In this work, we show that this is not the case. For the members of $AgPb_mSbTe_{m+2}$ family and based on the early reports on these systems, we expected them to form solid solutions between PbTe and $AgSbTe_2$ with the same symmetry and a statistical disorder of Ag−Sb−Pb atoms on the Na sites. Similarly for $AgPb_mSbTe_{m+2}$ we demonstrate that they possess a significant degree of ordering adopting lower symmetric space groups. We are going to elaborate on this issue by analyzing one by one the results obtained from the four characterization methods, namely X-ray powder diffraction, single-crystal X-ray diffraction, electron diffraction, and high-resolution imaging. We will begin with X-ray powder diffraction.

X-ray Powder Diffraction. As discussed above, no extra lines violating the F lattice are observed in the X-ray powder diffraction patterns, Figure 2. The variation of the cell parameters across different members of the $AgPb_mSbTe_{m+2}$ family suggests the members behave as typical solid solutions between $AgSbTe_2$ and PbTe. The plot in Figure 3 presents the cell parameters of $(AgSbTe_2)_{1-x}(PbTe)_x$ members as a function of *x*. The unit cell volume for several members of the family are plotted versus the *m* value and compared with the corresponding theoretical cell volume obtained by considering solid solutions between $AgSbTe_2$ and PbTe compounds.[27,28] There is good agreement between refined and calculated unit cell volumes. The compounds appear to obey Vegard's law with a parabolic deviation observed in most cases for solid solutions.[13,27] As we will show below however this picture is incorrect and misrepresents what actually is going on in these systems.

Single-Crystal X-ray Diffraction. Table 1 presents intensity statistics and relative intensity data of chosen reflections for the single-crystal samples studied in this work. If we compare the intensities of the weakest F-allowed reflection (331) observed in the powder pattern and the strongest reflection involving the P lattice (100), it is apparent that the P reflections, observed from single crystals, are too weak to appear in the X-ray powder diffraction patterns.

The structures of different members of the $AgPb_mSbTe_{m+2}$ family could be refined in the $Pm\bar{3}m$ space group as suggested by the *hkl* file showing an impressive number of reflections inconsistent with the F lattice (Table 1) and also could be refined in a lower symmetric space group such as $R\bar{3}m$ for $AgSbTe_2$ or $P4/mmm$ space groups for all compounds related to the cubic unit cell via cell transformations. The unit cell transformations from cubic $Fm\bar{3}m$ to tetragonal $P4/mmm$ and from cubic $Fm\bar{3}m$ to rhombohedral $R\bar{3}m$ with hexagonal axes are given by eqs 1

(26) Quarez, E.; Hsu, K.-F.; Hogan, T.; Short J.; Uher, C.; Kanatzidis, M. G. Manuscript in preparation.

(27) Urusov, V. S. *Zh. Strukt. Khim.* **1992**, *33*, 80−92.
(28) Kostikova, G. P.; Kostikov, Y. P. *Neorg. Mater.* **1993**, *29*, 1136−1137.

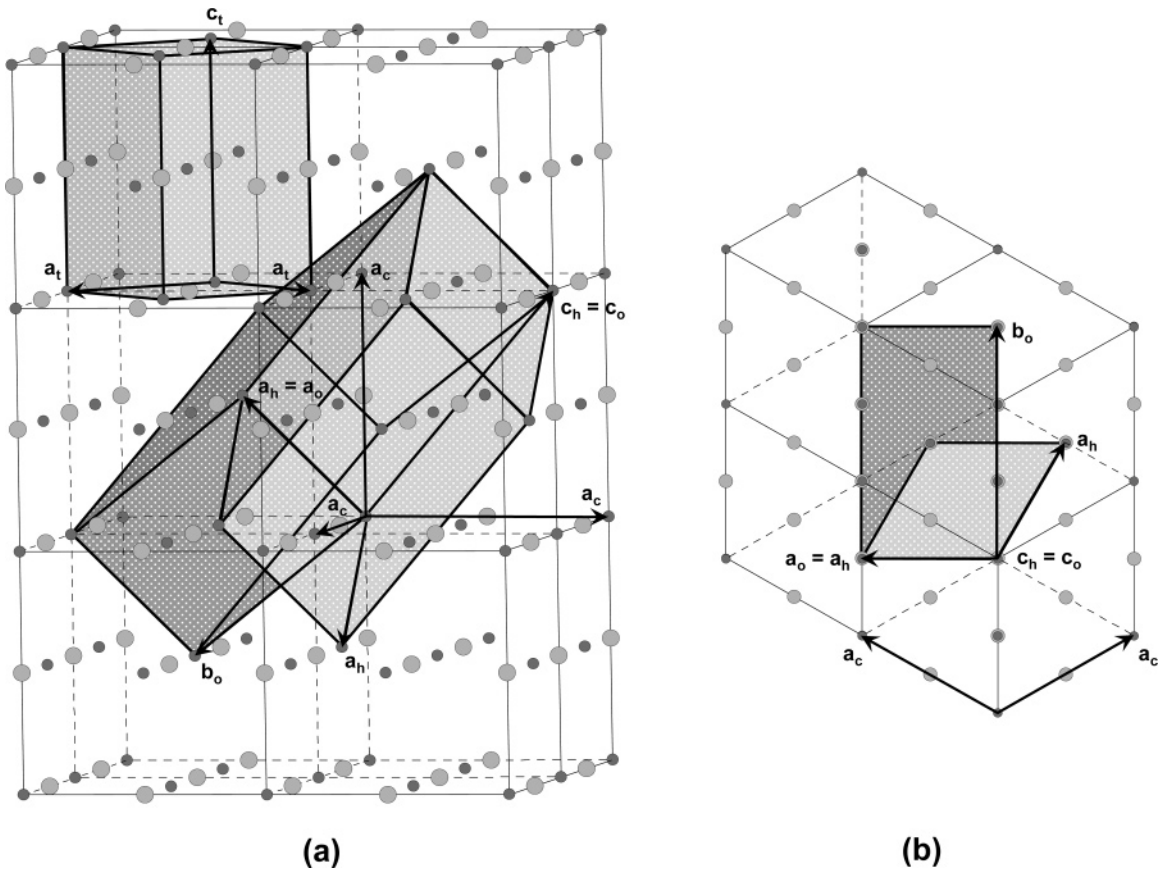

Figure 4. (a) Representation of the relations between cubic, tetragonal, hexagonal, and orthorhombic unit cells according to cubic to tetragonal unit cell: $a_t = b_t = a_c\sqrt{2}/2$ and $c_t = a_c$, cubic to hexagonal unit cell: $a_h = b_h = a_c\sqrt{2}/2$ and $c_h = a_c\sqrt{3}$ and cubic to orthorhombic unit cell: $a_o = a_h = a_c\sqrt{2}/2$, $b_o = a_h\sqrt{3} = a_c\sqrt{6}/2$, $c_o = c_h = a_c\sqrt{3}$. Figure 4b shows the same representation viewed down the [111] cubic direction.

and 2, respectively. Figure 4a is a schematic representation of the relations between cubic, tetragonal, and rhombohedral (hexagonal axes) unit cells.

$$\begin{pmatrix} a \\ b \\ c \end{pmatrix}_t = \begin{pmatrix} 0.5 & -0.5 & 0 \\ 0.5 & 0.5 & 0 \\ 0 & 0 & 1 \end{pmatrix} \times \begin{pmatrix} a \\ b \\ c \end{pmatrix}_c \quad (1)$$

$$\begin{pmatrix} a \\ b \\ c \end{pmatrix}_h = \begin{pmatrix} 0 & -0.5 & 0.5 \\ 0.5 & 0 & -0.5 \\ 1 & 1 & 1 \end{pmatrix} \times \begin{pmatrix} a \\ b \\ c \end{pmatrix}_c \quad (2)$$

When the crystal symmetry drops from $Fm\bar{3}m$ to $Pm\bar{3}m$ (or lower symmetry such as tetragonal $P4/mmm$ or trigonal $R\bar{3}m$), the number of unique sites in the unit cell doubles. For example, the Na site at $^1/_2$, $^1/_2$, $^1/_2$ splits into two in the tetragonal cell case, namely $^1/_2$, $^1/_2$, 0 and 0, 0, $^1/_2$. The X-ray refinements indicate that these two Na sites are occupied differentially by the various Ag, Sb, and Pb atoms which of course causes the symmetry breaking in the first place.

It is a very delicate choice to decide between the various models since all refinements are acceptable and can be disturbed because of the nature of the elements (coherent X-ray scattering amplitudes of Sb and Te atoms are almost identical and close to those of Ag). The first tendency was to choose the higher symmetric space group ($Pm\bar{3}m$), but according to the number of data and parameters, the tetragonal model was preferred for all cases. It is interesting that an ordered albeit small unit cell can be defined ($a = b \approx a_c\sqrt{2}/2$, $c \approx a_c$) which in fact gives a statistically better refinement suggesting this model has to be chosen over the $Pm\bar{3}m$ one described above. The statistically significant reductions in R_1 and wR_2 values of $Ag_{1.33}Pb_{1.33}Sb_{1.33}Te_4$, $Ag_{0.5}Pb_3Sb_{0.5}Te_4$, $Ag_{0.38}Pb_{3.23}Sb_{0.38}Te_4$, and $Ag_{0.25}Pb_{3.5}Sb_{0.25}Te_4$ (from (R_1/wR_2): 1.57/4.77, 2.73/5.40, 2.71/8.12, 2.08/4.72 in $Pm\bar{3}m$ to 1.12/3.23, 2.47/4.95, 2.37/7.30, and 2.09/4.69 in $P4/mmm$, respectively) are obtained with a larger number of data-to-parameter ratio, see Tables 2 and 3. For the single crystal of $AgSbTe_2$, the choice between $P4/mmm$ and $R\bar{3}m$ space groups (both preferable to $Pm\bar{3}m$) is more difficult to make since the R_1 and wR_2 for the $P4/mmm$ refinement (R_1 = 2.79% and wR_2 = 8.31%) are slightly lower than those for the $R\bar{3}m$ refinement (R_1 = 2.84% and wR_2 = 9.38%), whereas the number of data are higher in the case of $R\bar{3}m$ (267 against 225 for $P4/mmm$) for a different number of parameters (6 versus 8). Hamilton significance tests on the R_1 factor suggested the $P4/mmm$ space group choice as the model showing the best fit with the data.[29] This is the first time experimental evidence is presented that $AgSbTe_2$ is not a cubic compound or disordered NaCl-type but ordered tetragonal or possibly rhombohedral.[30] Interestingly, ab initio band structure calculations on both the tetragonal and rhombohedral models suggest the latter to be of slightly lower total energy.[31]

The crystal structures are depicted in Figure 5. For the structure of $AgSbTe_2$, both representations in the tetragonal and

(29) Hamilton, W. C. *Acta Crystallogr.* **1965**, *18*, 502−510.
(30) Any appearance of cubic behavior could be explained by the presence of multiple microtwinning.
(31) Bilc, D.; Quarez, E.; S. D. Mahanti; Kanatzidis, M. G. Work in progress.

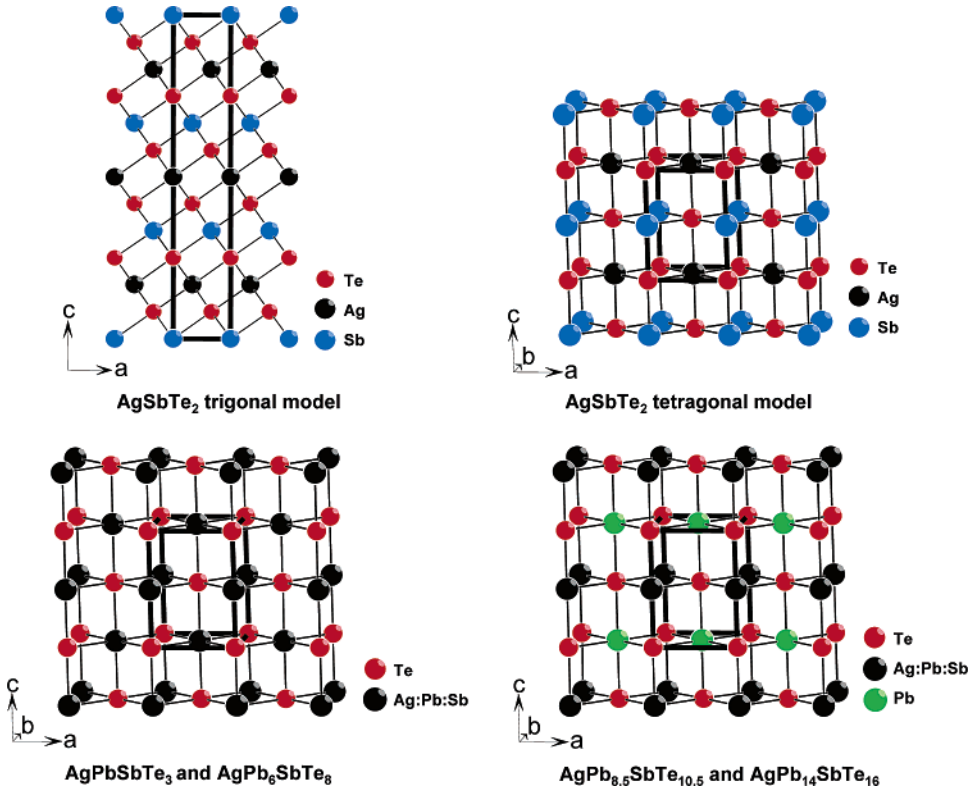

Figure 5. Graphical representation of the crystal structures showing the best fit with the data collection: $AgSbTe_2$ drawn in the $R\bar{3}m$ and $P4/mmm$ space groups; $Ag_{1.33}Pb_{1.33}Sb_{1.33}Te_4$, $Ag_{0.5}Pb_3Sb_{0.5}Te_4$, $Ag_{0.38}Pb_{3.23}Sb_{0.38}Te_4$, and $Ag_{0.25}Pb_{3.5}Sb_{0.25}Te_4$ in the $P4/mmm$ space group. In these four latter crystal structures, the mixed occupancy sites are indicated in black.

trigonal models are shown. In the $P4/mmm$ space group, AgTe and SbTe layers are packed along the c-axis. In the $R\bar{3}m$ space group, Ag and Sb atoms form layers alternating with Te layers along the c-axis. In the tetragonal structures of $AgPbSbTe_3$ and $Ag_{0.5}Pb_3Sb_{0.5}Te_4$, both cations sites are mixed occupied (black color) with occupancies detailed in Table 4. Finally, for $Ag_{0.38}Pb_{3.23}Sb_{0.38}Te_4$ and $Ag_{0.25}Pb_{3.5}Sb_{0.25}Te_4$, one of the cation sites is occupied by Ag, Pb, and Sb atoms, whereas the second one is occupied only by Pb atoms. The different occupations of Ag/Pb/Sb in the mixed sites reported in Table 4 led to the formulas summarized in Tables 2 and 3.

These results reveal at least a complete or partial ordering of Ag/Pb/Sb atoms at long range in the structure and provide proof that $AgPb_mSbTe_{m+2}$ members are not classical solid solutions. Considering that the single crystal X-ray refinements present only an average structure, it is possible that more extensive atomic ordering is actually present at the nanoscopic level. Given that such ordering originates from a high-symmetry archetypal structure (NaCl), multiple twinning could result at the nanoscopic scale which when averaged could give the appearance of $Pm\bar{3}m$ symmetry. For this reason, it was also worthy to study these compounds with methods able to analyze local areas such as electron diffraction and high-resolution imaging using TEM.

Electron Diffraction. Selected area electron diffraction (SAED) was performed on samples of $Ag_{0.95}Pb_{15}SbTe_{17}$ and $Ag_{0.86}Pb_{18}SbTe_{20}$. Electron diffraction patterns taken along several zone axes, from both compounds, showed similar features, and therefore we present results only for the $Ag_{0.95}Pb_{15}SbTe_{17}$ sample which was scrutinized more intensely. The figure of merit of the $Ag_{0.95}Pb_{15}SbTe_{17}$ sample was slightly lower than the $m = 18$ sample, but this sample remains "competitive" and worth studying.

Different areas on the $Ag_{0.95}Pb_{15}SbTe_{17}$ sample were analyzed (Figure 6), and depending on the location, the electron diffraction patterns exhibited different features. This indicated phase inhomogeneity at the nanoscopic level. Five different types of structural features were observed by electron diffraction:

1. patterns exhibiting a perfect cubic F lattice with cell parameter $a \approx 6.4$ Å (Figure 7) and sometimes accompanied with diffuse streaks (Figure 8a). These results are in agreement with $Fm\bar{3}m$ observed in the powder X-ray patterns of different member compounds. Diffuse streaks are an evidence for Ag, Sb, and Pb atoms tending to order but still are randomly arranged within the structure.

2. patterns showing extra spots that violate the F lattice (Figure 8b). The extra spots, highlighted by small white arrows, can be indexed to a cubic P unit cell with $a \approx 6.4$ Å. These results agree with the X-ray single-crystal diffraction results presented above.

3. patterns exhibiting splitting of spots which becomes larger the more we move away from the origin (Figure 8c). This feature is evidence of the coexistence of two phases in the same area with similar but not identical cell parameters and identical crystallographic orientation. The phase with the slightly smaller cell parameter is richer in Ag and Sb, whereas the phase with the longer cell parameter is correspondingly more rich in Pb. This observation strongly implies a well-defined compositional fluctuation in the material away from the average m value.

4. patterns showing supercell reflections characteristic of a doubling of the cubic unit cell $a \approx 12.8$ Å at least along one

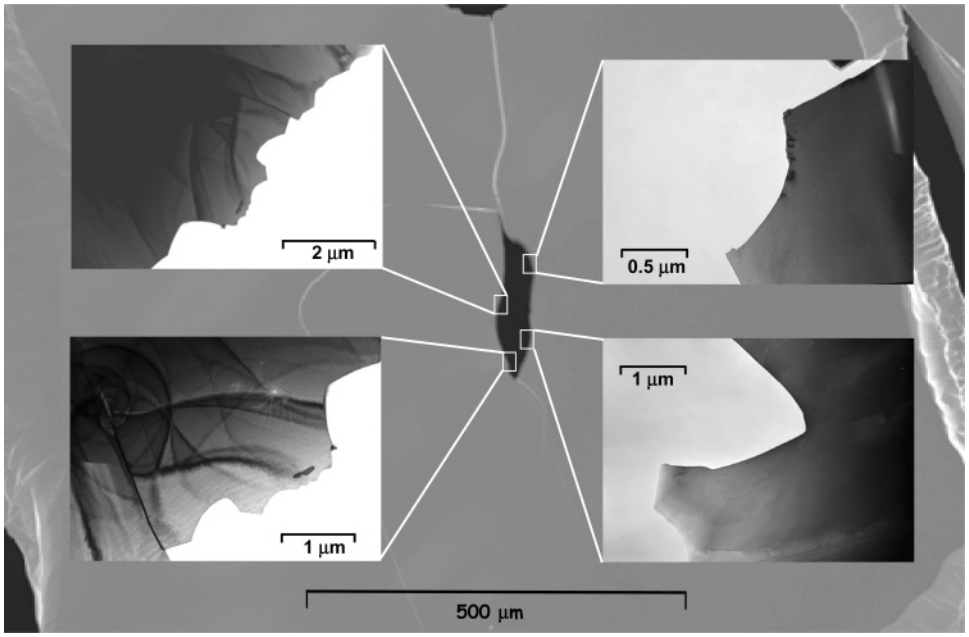

Figure 6. Examples of areas observed by transmission electron microscopy on a LAST-15 sample exhibiting different local structures as revealed by electron diffraction.

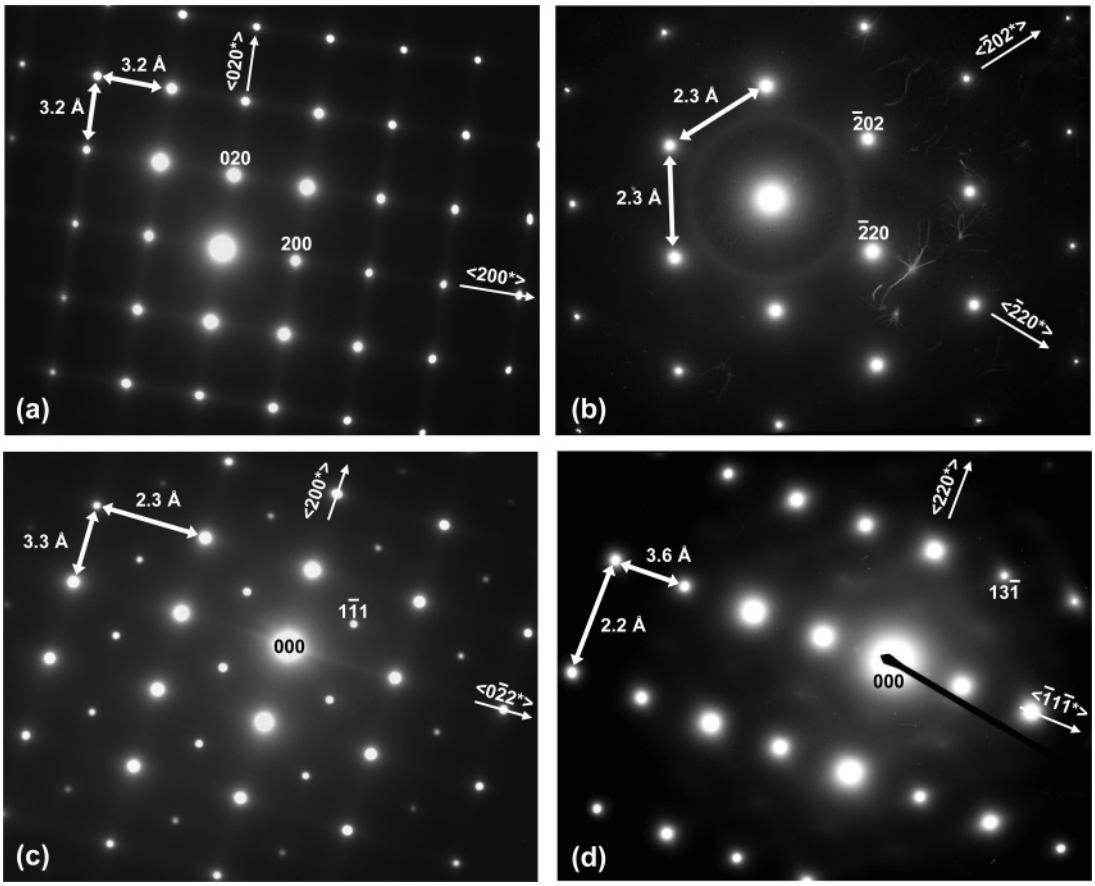

Figure 7. Selected area electron diffraction patterns (SAEDs) revealing a cubic F lattice viewed along four distinct crystallographic directions: (a) [001], (b) [111], (c) [011], and (d) [$\bar{1}$12]. Weak diffuse streaks can be observed on almost all patterns. Their diffuse nature is consistent with atomic disorder in this part of the sample.

crystallographic direction (Figure 8d). The [011] zone axis shown in Figure 7d exhibits extra diffraction spots indicated by the small white arrows and indexed to a possible F supercell of $a \approx 12.8$ Å.

5. finally, patterns exhibiting extra spots involving modification of the unit cell and reduction of the cubic symmetry (Figure 9a−d). Indeed, to index all spots, an orthorhombic unit cell that can be related to the parent cubic F unit cell via matrix

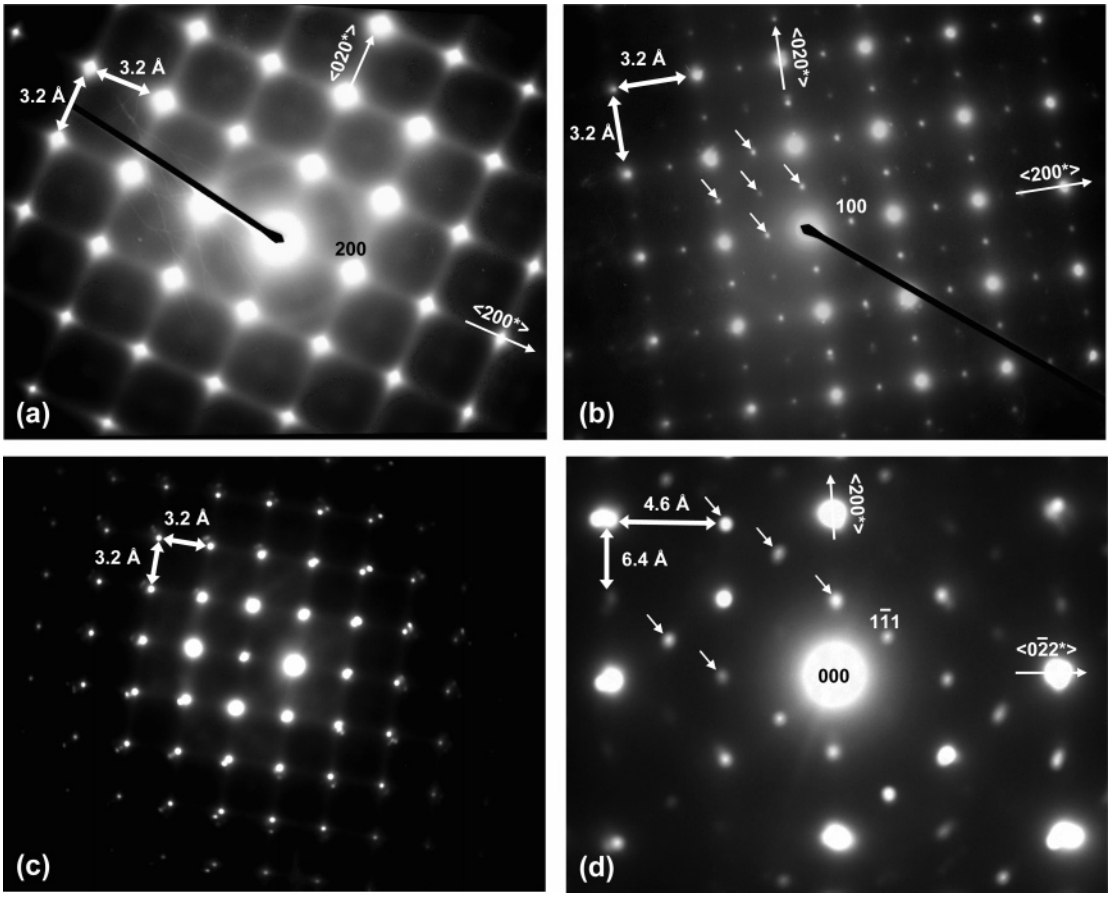

Figure 8. Examples of SAEDs exhibiting F centered lattice with additional features: (a) diffuse streaks on [001] zone axis, (b) supplementary spots (white arrows) on [001] zone axis violating the F lattice, (c) splitting spots on [001] zone axis highlighting multiphases with identical symmetry but different cell parameters, (d) extra spots (white arrows) on [011] zone axis leading doubling of the *a* cubic cell parameter; indexation is given in the supercell.

transformations is necessary. The cell parameters of the orthorhombic supercell are $a_o \approx 9.1$ Å, $b_o \approx 15.8$ Å, and $c_o \approx 22.3$ Å.

This supercell derives by symmetry breaking from $Fm\bar{3}m$ via $R\bar{3}m$ to P. The unit cell transformations from cubic $Fm\bar{3}m$ to rhombohedral $R\bar{3}m$ with hexagonal axes and from rhombohedral $R\bar{3}m$ to orthorhombic *P* are given by eqs 2 and 3, respectively. Equation 3 takes into account the doubling along the three axes of the orthorhombic unit cell. Figure 4a presents the relations between cubic, rhombohedral (hexagonal axes), and orthorhombic unit cells, and Figure 4b shows the same representation viewed down the [111] cubic direction.

$$\begin{pmatrix} a \\ b \\ c \end{pmatrix}_o = \begin{pmatrix} 2 & 0 & 0 \\ 2 & 4 & 0 \\ 0 & 0 & 2 \end{pmatrix} \times \begin{pmatrix} a \\ b \\ c \end{pmatrix}_h \qquad (3)$$

As part of an effort to describe the new orthorhombic superstructure that obviously comes from a long-range atomic ordering of Ag/Sb/Pb within the lattice, several structural models were generated with the program Cerius2[24] and their calculated electron diffraction patterns were compared to those observed experimentally (Figure 9). The starting point was to build a model in the primitive supercell ($a_o \approx 9.1$ Å, $b_o \approx 15.8$ Å, and $c_o \approx 22.3$ Å) and containing only Pb and Te atoms. Then, by substituting the Pb by Ag or Sb atoms in the structure and using the constrain of proper composition, we generated a variety of structural models whose calculated electron diffraction patterns were compared with the experimental ones. No assumptions concerning the space group of the supercell were made, and consequently the symmetry was initially set to be *P*1. Thus, 48 independent Pb atoms were likely to be replaced by Ag or Sb atoms giving rise to a significant number of possibilities.

To reduce the number of solutions to a few realistic ones, several physicochemical factors were taken into account:

(a) a composition as close to the nominal one of $AgPb_{15}SbTe_{17}$ as possible was sought.

(b) in order to achieve charge balance, the number of Ag atoms was set equal to the number of Sb atoms.

(c) the distribution of Ag and Sb atoms was such that they were kept as close to each other as possible (i.e., second neighbors).

After numerous attempts to generate calculated patterns that matched closely the experimental ones (Figure 9a, b, and d), it appears that several models could describe them decently. Indeed, due to the strong interaction of the electron beam with sample, multiple scattering events (secondary and dynamic scattering) can occur leading to a more difficult comparison. Moreover, as shown in the diffraction pattern of Figure 9c that corresponds to the [001] zone axis in the orthorhombic case, a second system of reflections along the 020 axis is observed. These features made selection of the perfect model difficult. However, some peculiarities, shared by all models were that the ordering of Ag and Sb atoms tended to form isolated parallel columns along the *a*-axis inside the structure. One of these

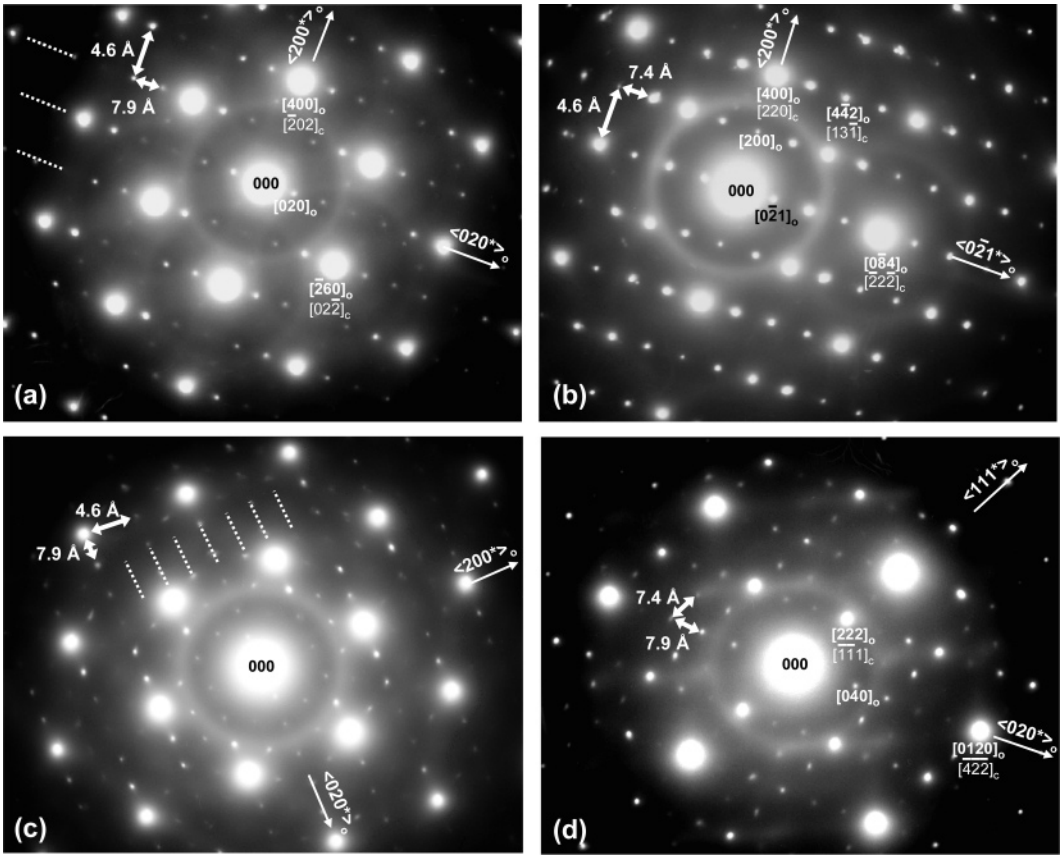

Figure 9. SAEDs showing a lowering of the crystal symmetry from cubic to orthorhombic. They correspond to (a and c) $[111]_c$, (b) $[\bar{1}12]_c$, and (d) $[\bar{2}31]_c$ zone axis in fcc symmetry ($a_c = 6.4$ Å). Superstructure spots can be indexed in orthorhombic symmetry according to $a_o \approx 9.1$ Å, $b_o \approx 15.8$ Å, and $c_o \approx 22.3$ Å unit cell. The corresponding zone axes are (a and c) $[001]_o$, (b) $[012]_o$, and (d) $[10\bar{1}]_o$. Indexations are given for both symmetries.

models showing the chains is shown in Figure 10. The nearby calculated SAEDs present two examples of orientations [001] and [012] deduced from this model and in good agreement with the experimental ones.

The electron diffraction studies clearly show the $AgPb_m$-$SbTe_{m+2}$ samples to possess different domains exhibiting nanostructures. This constitutes further definitive evidence that $AgPb_mSbTe_{m+2}$ members are not solid solutions. Finally, additional evidence was provided by high-resolution imaging.

High-Resolution Electron Microscopy (HREM) Images. Finally, high-resolution imaging performed on samples of $Ag_{0.86}$-$Pb_{18}SbTe_{20}$ clearly presents inhomogeneities at the nanoscopic level. Endotaxially embedded nanocrystals of varying sizes and shapes can be found in the samples. Two types of coherent nanodomains, showing different atomic spacings, can be observed in Figure 11a magnified in Figure 11b and c. Some domains show 12 Å spacings and a doubling of the periodicity. Fast Fourier transforms (FFT) of these domains yield a doubling of the cell parameter (Figure 11c). Neighboring domains show normal 6 Å spacings (Figure 11b). The doubling of the cell parameter encountered in Figure 11a can be associated with the results of electron diffraction which exhibit identical features on the same sample: patterns showing a unit cell of ~6.4 Å (Figure 7a−d) and patterns showing a double unit cell (Figure 8d). As suggested previously,[5] we can assume that the observed structural differences are the result of regions which are rich in Ag−Sb and regions poor in Ag−Sb leading to a situation that produces Ag−Sb-rich nanodots embedded in a Ag−Sb-poor matrix (i.e., rich in PbTe).

The coherent nature of these nanocrystals with the surrounding matrix is an important feature. We can view the nanocrystals as being endotaxially embedded in the matrix with a nearly perfect lattice match on all sides, as HREM images clearly reveal (Figure 12), although the matrix and the precipitate have a lattice mismatch of 2−5%. Dislocations are observed at the nanocrystal/matrix interface. This endotaxy occurring in these materials could be highly conducive to facile carrier transport throughout the sample. Therefore under proper carrier doping one could expect relatively high mobilities. At the same time the very high number of nanocrystal/matrix interfaces could provide a formidable barrier to phonon transmission in the bulk sample, thereby setting the foundation for a marked enhancement in ZT relative to that of the classical solid solution system.

In the case of LAST-18 ($AgPb_{18}SbTe_{20}$) member, HREM images were able to clarify the nature of the endotaxially grown nanodots. In Figure 13a, an HREM micrograph is presented showing a nanocrystal in the matrix. Figure 13b and c show the corresponding FFTs of the left and the right side of the image. It is clear that the left one corresponds to a cubic NaCl-type structure and the right one (due to the presence of extra spots along the one of the [100] axes) to a noncubic phase (possibly tetragonal or orthorhombic). Careful measurements from the image and the FFT reveal that the two lattice parameters of the precipitate, measured along the two cubic [100] directions, differ by approximately 2%.

The nanocrystal shown in the micrograph of Figure 14a appears with different features than the previous one. As it can be seen also from the corresponding FFT (Figure 14b) extra

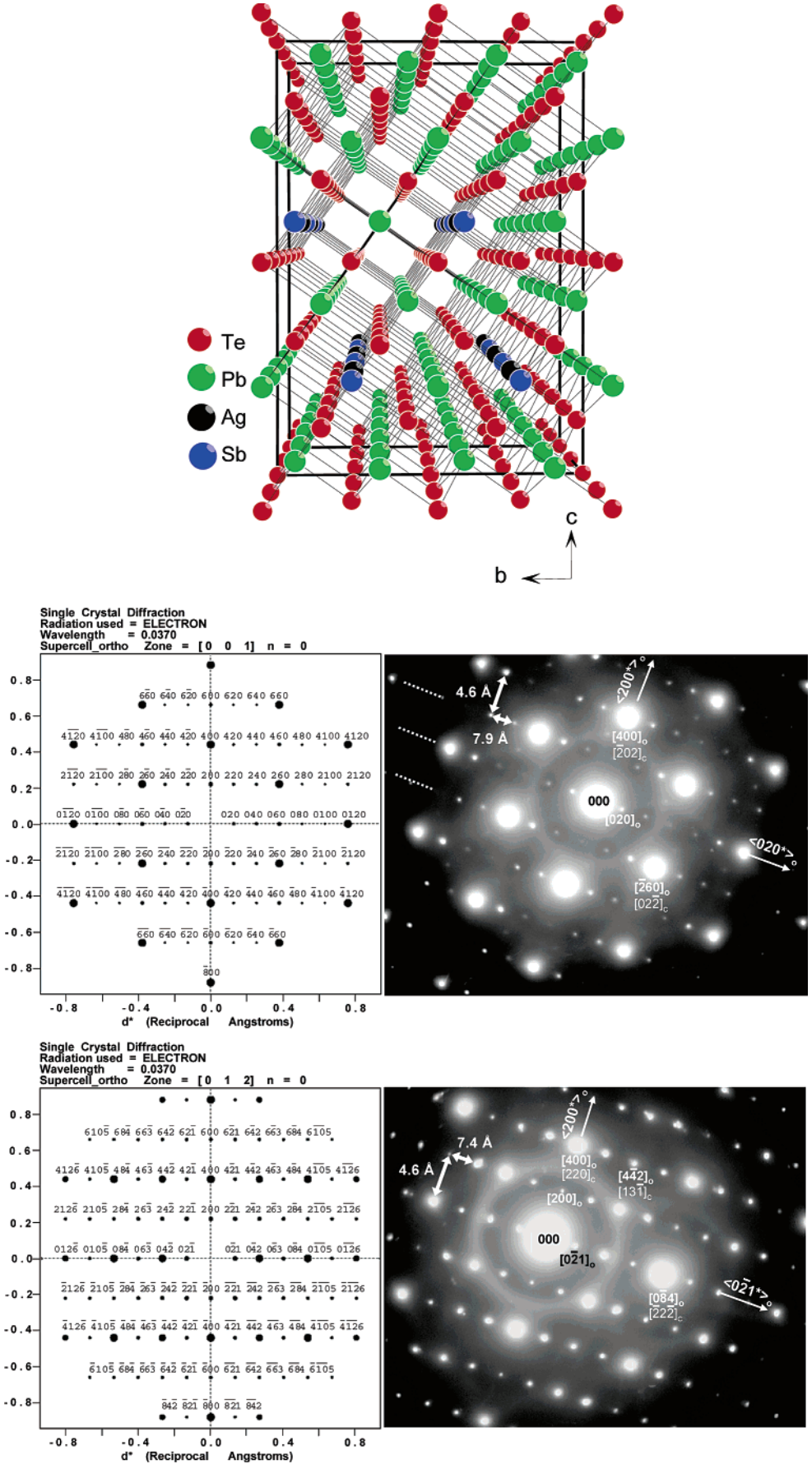

Figure 10. Example of structural model highlighting the isolated parallel Ag−Sb chains within the structure. The nearby calculated SAEDs present two examples of orientations $[001]_o$ and $[012]_o$ deduced from this model and in good agreement with the experimental ones.

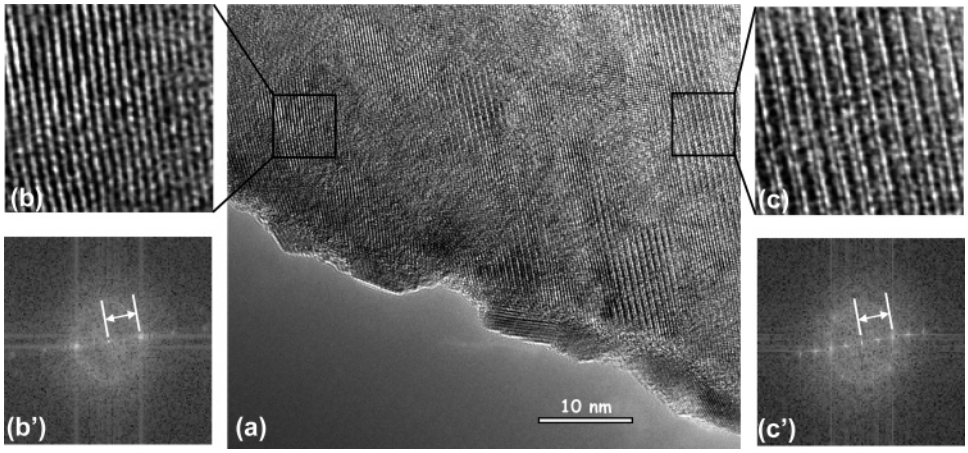

Figure 11. High-resolution image on a LAST-18 sample (a) showing the coexistence at the nanoscopic scale of two kinds of domains magnify in b and c figures. The fast Fourier transforms (FFT) of such zones (b′ and c′, respectively) show that the cell parameter of domain c is double than that of domain b.

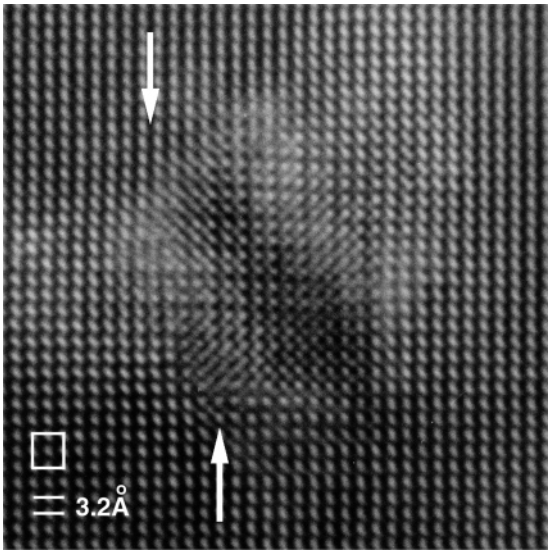

Figure 12. HREM image from an LAST-18 sample showing the endotaxial growth of a nanocrystal in the matrix. The electron beam is parallel to one of the [100] directions. A unit cell is indicated. The presence of dislocations at the nanocrystal/matrix interface is indicated by arrows.

spots appear along both the *a**- and *b**- axes. It is probably the cubic phase with P symmetry described above. However in some cases a very small difference (1−2%) between the two cubic axes was measured, denoting probably the lowering of the symmetry from cubic to tetragonal or orthorhombic.

Conclusion

We have presented here direct proof that the $AgPb_mSbTe_{m+2}$ samples do not behave as classical solid solutions between $AgSbTe_2$ and PbTe but exhibit nanoscopic inhomogeneities with a large range of structural features from atomic ordering, revealed by single-crystal X-ray diffraction, to nanostructures highlighted by electron diffraction and high-resolution imaging. The superior thermoelectric figure of merit in the LAST materials by a large part originates from a lowering of the lattice thermal conductivity. The presence of coherent, endotaxial, nanosized islands that are rich in Ag−Sb embedded in a matrix rich in Pb may be associated with the enhancement of the thermoelectric properties encountered in the $AgPb_mSbTe_{m+2}$ materials. One of the possible explanations for the depression of the thermal conductivity with simultaneous retention of a high power factor is that these coherent nanocrystalline regions possess different electronic and vibrational properties than those of the surrounding matrix leading to a sort of quantum confinement and enhanced acoustic phonon scattering.[32] From these considerations it becomes apparent that the thermoelectric properties of the LAST family of materials might be very sensitive to the experimental conditions employed to prepare them. If proper conditions prevail to allow these nanostructures to develop we may anticipate superior thermoelectric properties.

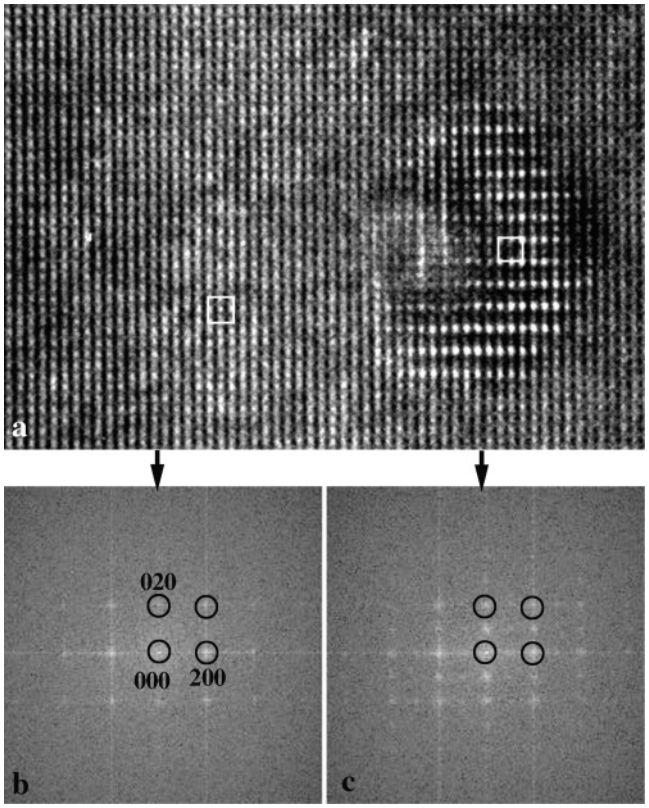

Figure 13. HREM image from an LAST-18 sample (a) and the FFTs from the matrix (b) and the nanocrystal (c). The electron beam is parallel to one of the [100] directions. The unit cells are indicated.

(32) (a) Hicks L. D.; Dresselhaus M. S. *Phys. Rev. B* **1993**, *47*, 12727−12731. (b) Hicks L. D.; Harman T. C.; Dresselhaus M. S. *Appl. Phys. Lett.* **1993**, *63*, 3230−3232. (c) Dresselhaus M. S.; Lin Y. M.; Cronin S. B.; Rabin O.; Black M. R.; Dresselhaus G.; Koga T. *Recent Trends In Thermoelectric Materials Research* Iii Semiconductors and Semimetals **2001**, *71*, 1−121.

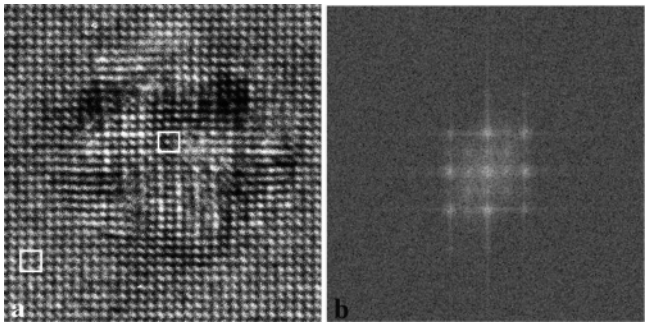

Figure 14. HREM image from an LAST-18 sample (a) and the corresponding FFT's from nanocrystal (b). The electron beam is parallel to one of the [100] directions. The image and the FFT have different features than the previous one (Figure 13).

However a change in the structural order/disorder balance and atomic mass fluctuation from what is optimum for low thermal conductivity may lead to different thermoelectric behavior. The results reported here provide experimental evidence for a conceptual basis to employ when designing high performance thermoelectric materials. A major future challenge will be to control the coherence, the size and the proportion of the nanostructures within the matrix in order to determine precisely their impact on the thermoelectric properties. Such nanostructure control could enable a substantial suppression of the thermal conductivity without considerably altering the power factor.

Acknowledgment. Financial support from the Office of Naval Research (Contract No. N00014-02-1-0867 MURI program) is gratefully acknowledged. We thank Professor S. D. Mahanti and D. Bilc for fruitful discussions. The 200 kV Field Emission Gun Transmission Electron Microscope was acquired with an NSF grant (DMR-0079578) (MSU Center for Advanced Microscopy).

Supporting Information Available: X-ray crystallographic files in CIF format for single crystals of $AgSbTe_2$ $Ag_{1.33}Pb_{1.33}Sb_{1.33}Te_4$, $Ag_{0.5}Pb_3Sb_{0.5}Te_4$, $Ag_{0.38}Pb_{3.23}Sb_{0.38}Te_4$, and $Ag_{0.25}Pb_{3.5}Sb_{0.25}Te_4$. This material is available free of charge via the Internet at http://pubs.acs.org.

JA051653O